

Realizing a tunable honeycomb lattice in ABBA-stacked twisted double bilayer WSe₂

Haining Pan¹, Eun-Ah Kim^{1,2,3,4} and Chao-Ming Jian¹

¹Department of Physics, Cornell University, Ithaca, New York 14850, USA

²Radcliffe Institute for Advanced Studies, Cambridge, Massachusetts, USA

³Department of Physics, Harvard University, Cambridge, Massachusetts 02138, USA

⁴Department of Physics, Ewha Womans University, Seoul 03760, South Korea



(Received 25 July 2023; revised 19 October 2023; accepted 24 October 2023; published 27 November 2023)

The ideal honeycomb lattice, featuring sublattice and SU(2) spin rotation symmetries, is a fundamental model for investigating quantum matter with topology and correlations. With the rise of the moiré-based design of model systems, realizing a tunable and symmetric honeycomb lattice system with a narrow bandwidth can open access to new phases and insights. We propose the ABBA-stacked twisted double bilayer WSe₂ as a realistic and tunable platform for reaching this goal. Adjusting the twist angle allows the bandwidth and the ratio between hopping parameters of different ranges to be tuned. Moreover, the system's small bandwidth and spin rotation symmetry enable effective control of the electronic structure through an in-plane magnetic field. We construct an extended Hubbard model for the system to demonstrate this tunability and explore possible ordered phases using the Hartree-Fock approximation. We find that at a hole filling of $\nu = 2$ (two holes per moiré unit cell), an in-plane magnetic field of a few tesla can “dope” the system from a semimetal to a metal. Interactions then drive an instability towards a canted antiferromagnetic insulator ground state. Additionally, we observe a competing insulating phase with sublattice charge polarization. Finally, we discuss the experimental signatures of these insulating phases.

DOI: [10.1103/PhysRevResearch.5.043173](https://doi.org/10.1103/PhysRevResearch.5.043173)

I. INTRODUCTION

The ideal honeycomb lattice with both sublattice and SU(2) spin rotation symmetries is an important platform for studying many-body physics with topology and electronic correlations. Graphene has been widely studied as a material realization of this lattice. Yet, the system's wide bandwidth limits the exploration of the full phase space of honeycomb lattice systems. Realizing a symmetric honeycomb lattice with a narrow bandwidth and enhanced tunability would significantly expand the accessible phase space, enabling the exploration of higher doping levels and stronger correlations. Among other possibilities, this advancement would facilitate experimental investigations of various intriguing correlated phases proposed earlier, such as charge and spin density waves [1–3], chiral superconductivity [4,5], and topological Mott insulators [6]. Over the past few years, moiré superlattices in transition metal dichalcogenide (TMD) multilayer structures have emerged as a highly tunable platform for quantum simulation of two-dimensional lattice models with narrow bandwidth [7–21]. Triangular superlattices [7–14] and honeycomb superlattices with spin-orbit coupling (SOC) or asymmetric sublattices [14,19,21–23] have been realized. In this paper, we aim to find a twisted TMD multilayer structure that realizes an

ideal honeycomb lattice with both sublattice and SU(2) spin rotation symmetries.

Theoretically, a strategy to create an ideal emergent honeycomb lattice with sublattice and SU(2) spin symmetries in TMD multilayer structures follows three criteria as first pointed out in Refs. [24–26]: (1) The Γ valley of each TMD layer, where SOC is negligible, appears at the valence band edge (rather than the K and K' valleys), forming an emergent lattice for the doped holes [24–27]; (2) a symmetry relates the independent high-symmetry-stacking MX and XM sites [see Fig. 1(b)], which form the two sublattices of the emergent honeycomb lattice; and (3) the energy at the MX and XM sites is higher than that at the MM site (another high-symmetry stacking location) [28]. However, previous papers only proposed these strategies in TMD bilayers. The correct energetics [in criteria (1) and (3)] in these proposals are yet to be confirmed and realized by experiments. For example, Refs. [29,30] have experimentally identified the Γ -valley physics in twisted bilayer WSe₂ but found it to appear at energies much below the valence band edge, which is located at the K and K' valleys.

Here, we pursue realizing an ideal emergent honeycomb lattice in ABBA-stacked twisted double bilayer WSe₂ (tdbWSe₂), i.e., two AB- and BA-stacked WSe₂ bilayers with a small relative twist angle [see Fig. 1(a)]. As experimentally shown in a closely related system, the ABAB-stacked tdbWSe₂, the increase in the number of layers enhances the interlayer hybridization driving the Γ valley to the valence band edge [27,31]. However, the ABAB-stacked tdbWSe₂ does not have the symmetry needed for criterion (2) and only

Published by the American Physical Society under the terms of the [Creative Commons Attribution 4.0 International](https://creativecommons.org/licenses/by/4.0/) license. Further distribution of this work must maintain attribution to the author(s) and the published article's title, journal citation, and DOI.

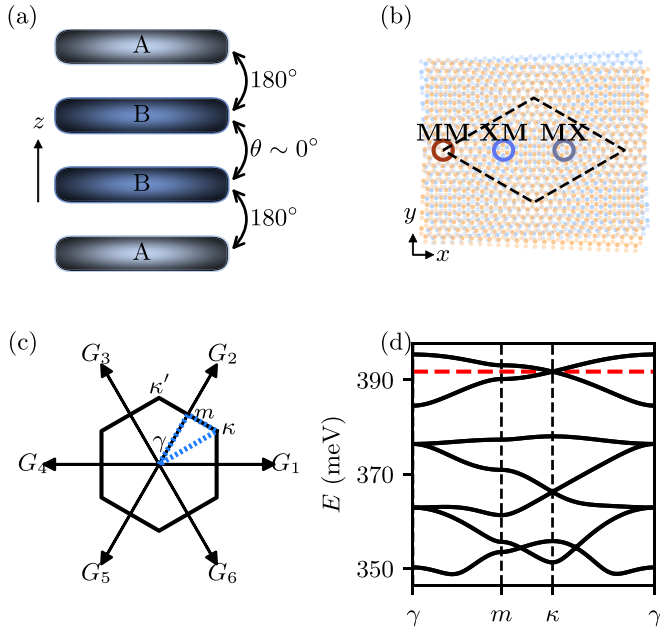


FIG. 1. (a) A schematic picture of the ABBA-stacked tdbWSe₂. Within each of the AB- and BA-stacked bilayers of WSe₂, the orientation of the two layers differs by 180°. The two bilayers are twisted so that the middle two layers have a small twist angle θ between them. (b) The real-space moiré pattern created by the twisted central two layers (blue and orange) with the darker (lighter) shade of color for the metal (chalcogenide) atom. The three high-symmetry-stacking sites in one moiré unit cell (black dashed lines) are *MM* (brown; metal atoms on one layer aligned with metal atoms on the adjacent layer), *XM* (blue; chalcogenide atom on one layer aligned with metal atoms on the adjacent layer), and *MX* (gray; metal atom on one layer aligned with chalcogenide atoms on the adjacent layer). Here, the alignment of atoms refers to the central two layers in the double bilayer structure. (c) Moiré Brillouin zone with four high-symmetry points γ , m , κ , and κ' . $G_{1,\dots,6}$ are the moiré reciprocal vectors. (d) Moiré band structure obtained from the continuum model at twist angle $\theta = 2^\circ$ along the path γ - m - κ - γ [blue dashed line shown in (c)]. The red dashed line indicates Fermi energy at hole filling $\nu = 2$ (two holes per moiré unit cell).

realizes a Γ -valley-based emergent triangular lattice. In this paper, we show that the ABBA-stacked tdbWSe₂ can pass the three criteria and realize a tunable ideal honeycomb lattice with both sublattice and SU(2) spin rotation symmetries.

The remainder of this paper is organized as follows. In Sec. II, we provide the microscopic analysis that the ABBA-stacked tdbWSe₂ can pass the three criteria above and, hence, leads to an emergent honeycomb lattice with both sublattice and SU(2) spin rotation symmetries. We construct a continuum model for this tdbWSe₂ system, enabling estimations of the hopping parameters of the emergent honeycomb lattice. In Sec. III, we demonstrate the intriguing tunability of this system by studying orders induced by an *in-plane* magnetic field at the hole filling $\nu = 2$, namely, the half filling of the emergent honeycomb lattice. The phase diagram is obtained using the Hartree-Fock analysis of the extended Hubbard model on the emergent honeycomb lattice. Finally, in Sec. IV, we summarize our results and experimental signatures of the predicted orders.

II. MODELING THE EMERGENT HONEYCOMB LATTICE

The ABBA-stacked tdbWSe₂ can satisfy the three criteria above for the following reasons. First, this structure's increased number of layers leads to stronger interlayer tunnelings compared with a single bilayer, pushing the Γ valley to the top of the valence bands [32,33]. Second, inherited from the D_{3h} point group symmetry of each WSe₂ layer, the ABBA-stacked tdbWSe₂ manifests a threefold rotation C_{3z} around the z axis, and a twofold rotation C_{2y} around the in-plane y axis, where the y axis is chosen to align with the xy -plane projection of a bond between the tungsten atom and the selenium atom in the monolayer WSe₂. These crystal symmetries ensure a sublattice-symmetric honeycomb lattice composed of the *MX* and *XM* sites. Third, from the *ab initio* tight-binding model in Appendix A, we find the correct energy hierarchy among the *MX*, *XM*, and *MM* sites to ensure an emergent honeycomb lattice.

To estimate the hopping parameters in the emergent honeycomb lattice based on the three criteria, we need to obtain the dispersion of the two topmost moiré valence bands. Adapting the approach in Refs. [25,31], we begin with a four-layer continuum Hamiltonian for our twisted ABBA-stacked system that preserves C_{2y} , C_{3z} , time-reversal, and SU(2) spin rotation symmetries (due to negligible SOC near the Γ valley [34]):

$$H_{4L} = -\frac{\hbar^2 \mathbf{k}^2}{2m} + \begin{pmatrix} \Delta_1(\mathbf{r}) & \Delta_{12}(\mathbf{r}) & 0 & 0 \\ \Delta_{12}^\dagger(\mathbf{r}) & \Delta_2(\mathbf{r}) & \Delta_{23}(\mathbf{r}) & 0 \\ 0 & \Delta_{23}^\dagger(\mathbf{r}) & \Delta_3(\mathbf{r}) & \Delta_{34}(\mathbf{r}) \\ 0 & 0 & \Delta_{34}^\dagger(\mathbf{r}) & \Delta_4(\mathbf{r}) \end{pmatrix}. \quad (1)$$

H_{4L} is identical for both spin species. The intralayer potentials take the forms $\Delta_1(\mathbf{r}) = \Delta_4(\mathbf{r}) = V_1$ for the first and fourth layers and $\Delta_2(\mathbf{r}) = V_2^{(0)} + 2V_2^{(1)} \sum_{i=1,3,5} \cos(\mathbf{G}_i \cdot \mathbf{r} + \phi)$ and $\Delta_3(\mathbf{r}) = V_2^{(0)} + 2V_2^{(1)} \sum_{i=1,3,5} \cos(\mathbf{G}_i \cdot \mathbf{r} - \phi)$ for the second and third layers (the opposite sign of ϕ as a result of C_{2y} symmetry). The interlayer tunnelings take the forms $\Delta_{12}(\mathbf{r}) = \Delta_{34}(\mathbf{r}) = V_{12}$ and $\Delta_{23}(\mathbf{r}) = V_{23}^{(0)} + 2V_{23}^{(1)} \sum_{i=1,3,5} \cos(\mathbf{G}_i \cdot \mathbf{r})$. Here, $\mathbf{G}_i = \frac{4\pi}{\sqrt{3}a_M} (\cos(\frac{(i-1)\pi}{3}), \sin(\frac{(i-1)\pi}{3}))$ for $i = 1, 2, \dots, 6$ are the six first-shell moiré reciprocal lattice vectors [see Fig. 1(c)]. The moiré lattice constant a_M is determined by the small twist angle θ through $a_M \approx a_0/\theta$ with the lattice constant a_0 of monolayer WSe₂ being 3.28 Å [35]. At $\theta \sim 2^\circ$, $a_M \approx 10$ nm. We adopt the effective mass $m = 1.2m_e$ with m_e being the electron rest mass [27,31]. The moiré reciprocal lattice vectors \mathbf{G}_i only show up in $\Delta_2 = \Delta_3$ and Δ_{23} because the small-angle twisting only appears between the second and third layers of WSe₂ in the twisted double bilayer structure.

We now estimate the parameters in the intralayer potentials and interlayer tunnelings in Eq. (1). These potentials and tunnelings in the tdbWSe₂ evaluated at the *MM*, *MX*, and *XM* sites should be fitted according to the band structures of the *untwisted* ABBA-stacked double bilayer WSe₂ in the three high-symmetry stacking configurations *MM*, *MX*, and *XM* (see Appendix A for more details) [36]. The angle-independent parameters for the potentials and tunnelings are estimated as follows: $(V_1, V_2^{(0)}, V_2^{(1)}) = (200, -159, -8)$ meV, $\phi = -0.17$, and $(V_{12}, V_{23}^{(0)}, V_{23}^{(1)}) =$

(184, 356, -9) meV. We comment that these parameter estimates are obtained based on assumptions about the interlayer distances in the double bilayer WSe₂ detailed in Appendix A. The assumed interlayer distances produce a representative example of tdbWSe₂ satisfying the energetics criteria allowing us to estimate the bandwidth and demonstrate the tunability of the emergent honeycomb lattice, which are the main purposes of our work. With the above parameters, we can solve Hamiltonian (1) for the moiré valence bands of tdbWSe₂. For example, Fig. 1(d) shows the band structure along the γ - m - κ - γ path in the moiré Brillouin zone (mBZ) at a twist angle of $\theta = 2^\circ$. From the two topmost moiré valence bands, especially the presence of a Dirac cone between them, we confirm that ABBA-stacked tdbWSe₂ with a hole filling of less than four holes per moiré unit cell captures an emergent honeycomb lattice with both sublattice and SU(2) spin rotation symmetries. At a twist angle of $\theta = 2^\circ$, the bandwidth is around 10 meV (which is much smaller than the ~ 2 eV bandwidth of graphene [37]).

At hole filling $\nu = 2$, i.e., two holes per moiré unit cell, the Fermi level is precisely at the Dirac point protected by C_{3z} and C_{2y} symmetries. This results in a semimetal (noninteracting) ground state, as shown in Fig. 1(d). The narrow bandwidth of the tdbWSe₂-realized honeycomb lattice allows for an intriguing way to tune the electronic structure: a realistic in-plane magnetic field can “dope” the semimetal and create finite Fermi surfaces located around both κ and κ' points of the mBZ for both spin species. Note that such tuning is impossible for the K -and- K' -valley-based TMD moiré system due to the strong SOC therein. The “doping” under the in-plane magnetic field is the result of the Zeeman effect. The thinness of the double bilayer structure allows us to ignore the orbital effect of the in-plane field. Without loss of generality, we assume that the in-plane magnetic field B is applied along the x direction, resulting in a Zeeman energy of $h_x = \frac{1}{2}g\mu_B B$, where μ_B is the Bohr magneton (5.79×10^{-2} meV/T), and the g factor is roughly 2 due to the negligible SOC near the Γ valley. For example, at a twist angle of $\theta = 2^\circ$, a magnetic field of 13 T, typically achievable experimentally, creates a Zeeman splitting energy of 0.8 meV. This Zeeman splitting leads to a finite Fermi surface of each spin species roughly halfway in energy between the Dirac point (at the κ point in the mBZ) and the van Hove singularity (at the m point), as shown in Fig. 2. In the presence of the in-plane field, a magnetic particle-hole instability that opens a charge gap is expected even at weak interactions because of the nesting between the Fermi surfaces of the two spin species. This instability would lead to a magnetic order that spontaneously breaks the remaining U(1) spin rotation symmetry about the x axis, namely, the in-plane field direction.

Conceptually, a similar in-plane-field-induced particle-hole instability applies to graphene. Previous work [3] shows that the resulting state is a canted Néel antiferromagnetic (AFM) insulator, whose magnetizations projected onto the plane perpendicular to the applied field are opposite in the two sublattices of the honeycomb. However, realizing such a state in graphene requires a very high in-plane field of $\sim 10^2$ – 10^3 T [3]. As we show below, a similar canted Néel AFM insulator can be found in the tdbWSe₂-realized honey-

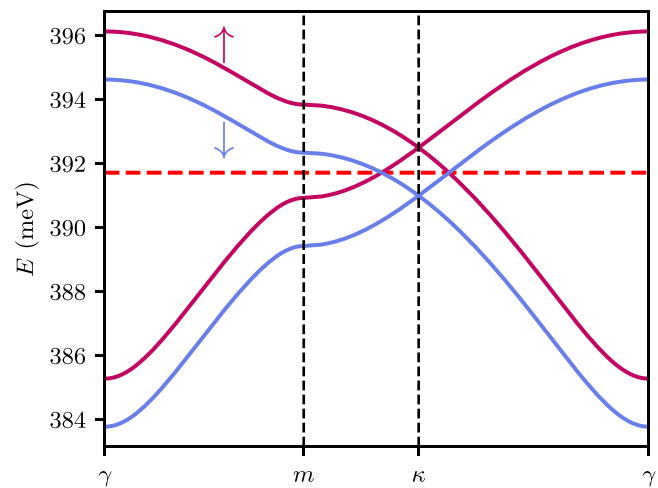


FIG. 2. The two topmost moiré valence bands shown in Fig. 1(d) split by the Zeeman energy shift due to an in-plane magnetic field of 13 T. The arrows indicate the spin along the in-plane field direction. The red dashed line indicates the Fermi energy at hole filling $\nu = 2$, i.e., two holes per moiré unit cell and half filling for the emergent honeycomb lattice.

comb lattice, whose bandwidth is engineered around the meV scale, at a realistic in-plane field of a few tesla.

III. EXTENDED HUBBARD MODEL AND PHASE DIAGRAM UNDER AN IN-PLANE FIELD

Aside from the bandwidth distinction with graphene, the band structure of the tdbWSe₂-realized honeycomb lattice exhibits a more pronounced contribution from the next-nearest-neighbor (NNN) hopping t_2 on the honeycomb lattice. The effect of t_2 is manifested by the asymmetry (about the Dirac cone) between the two topmost valence bands shown in Fig. 1(d). In contrast to the graphene-inspired model of Ref. [3] with only the nearest-neighbor (NN) hopping t_1 and the on-site Hubbard interaction, we consider an extended Hubbard model with longer-range hoppings and interactions pertaining to our tdbWSe₂-realized honeycomb lattice system. Our Hamiltonian consists of three terms: the hopping H_h , the Zeeman energy H_Z from the in-plane magnetic field, and the extended Hubbard interaction H_{int} . The term $H_h = -t_1 \sum_{\langle ij \rangle} \sum_{\sigma} c_{i\sigma}^{\dagger} c_{j\sigma} - t_2 \sum_{\langle\langle ij \rangle\rangle} \sum_{\sigma} c_{i\sigma}^{\dagger} c_{j\sigma}$ contains both NN hopping t_1 and NNN hoppings t_2 . Here, $c_{i\sigma}$ is the fermion operator of the hole with spin σ at site i of the emergent honeycomb lattice. Both t_1 and t_2 are real because of the SU(2) spin rotation symmetry and the time-reversal symmetry. t_1 and t_2 are tunable by the twist angle θ . For instance, at $\theta = 2^\circ$, we estimate $t_1 = 1.8$ meV and $t_2 = 0.2$ meV based on the moiré band structure obtained from the continuum model equation (1). The ratio t_2/t_1 varies as we change the twist angle: 0.018 for $\theta = 1^\circ$, 0.11 for $\theta = 2^\circ$, and 0.12 for $\theta = 3^\circ$. In the search for possible phases below, we treat t_2/t_1 as a parameter to explore the effect of longer-range hopping. The Zeeman energy H_Z is given by $H_Z = h_x \sum_i (c_{i\uparrow}^{\dagger} c_{i\uparrow} - c_{i\downarrow}^{\dagger} c_{i\downarrow})$, where the spin quantization axis conveniently is chosen along the x direction. Under H_Z , the spin symmetry is reduced to a U(1) spin rotation in the yz plane. We fix $h_x = 0.4t_1$ in the

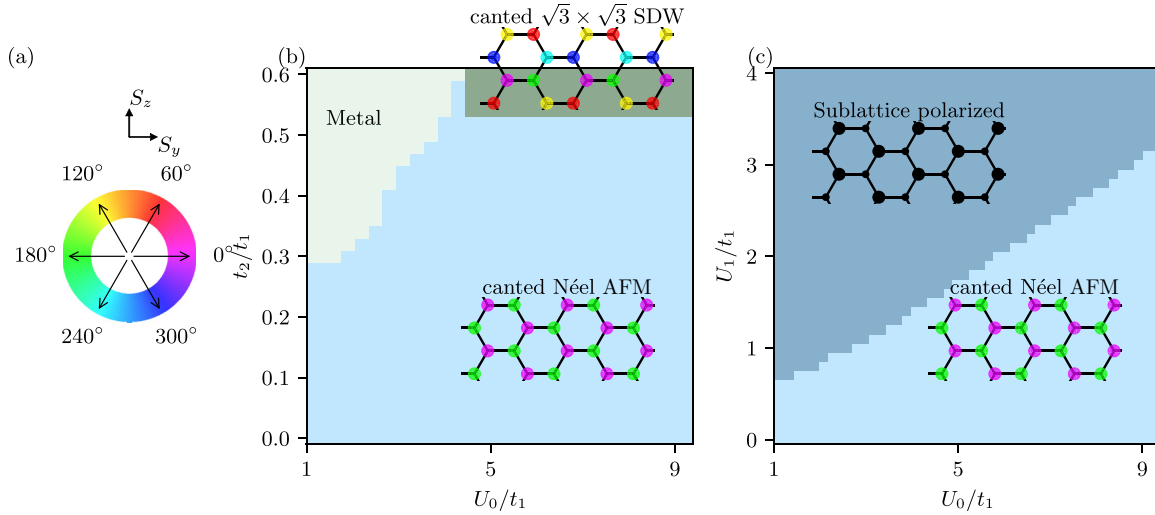


FIG. 3. (a) The color wheel shows the six spin orientations in the yz plane. (b) The phase diagram as a function of U_0 and t_2 . (c) The phase diagram as a function of U_0 and U_1 . Here, the size of the dot indicates the number density of each site, while the color indicates the spin orientation in the yz plane as shown in the color wheel. The black dots in the sublattice-polarized state indicate zero spin polarization.

following. For the twist angle $\theta = 2^\circ$, $h_x = 0.4t_1$ (corresponding to a 13 T in-plane magnetic field) sets the Fermi level roughly halfway between the Dirac point at the κ or κ' point and the Van Hove singularity at the m point of the mBZ.

The range of interactions in TMD-based superlattices typically extends beyond on-site interactions. Here, we consider the extended Hubbard interaction

$$H_{\text{int}} = U_0 \sum_i c_{i\uparrow}^\dagger c_{i\uparrow} c_{i\downarrow}^\dagger c_{i\downarrow} + U_1 \sum_{\langle ij \rangle} \sum_{\sigma, \sigma' = \uparrow, \downarrow} c_{i,\sigma}^\dagger c_{i,\sigma} c_{j,\sigma'}^\dagger c_{j,\sigma'}, \quad (2)$$

with the on-site interaction strength U_0 and the NN Hubbard interaction of strength U_1 . In the following study of the phase diagram, we treat U_0 and U_1 as two free parameters to explore their effect on the canted Néel AFM insulator and other phases.

We start with understanding the effect of the NNN hopping t_2 and present the ground-state phase diagram obtained using the Hartree-Fock method in Fig. 3(b). In this phase diagram, we consider a parameter range $U_0 \in [t_1, 9t_1]$ and $t_2 \in [0, 0.6t_1]$ while setting $U_1 = 0$. Using the numerical Hartree-Fock method, we find three possible phases: the canted Néel AFM insulator, a canted $\sqrt{3} \times \sqrt{3}$ spin density wave (SDW), and a metal. At hole filling $\nu = 2$, the Fermi surfaces of the two spin species are always perfectly nested for $t_2 \lesssim t_1/3$ at both the κ and κ' points of the mBZ. This perfect nesting results in a Fermi surface instability towards a robust canted Néel AFM insulator, spontaneously breaking the $U(1)$ spin rotation symmetry in the yz plane as mentioned above. Beyond $t_2 > t_1/3$, the system's ground state is metallic at small U_0 . The metallic state is due to an extra Fermi surface of the spin-down hole appearing around the γ point when $t_2 > t_1/3$. Consequently, the Fermi surfaces of the two spin species are no longer nested at $\nu = 2$. As U_0 increases, the system can enter an insulating SDW phase with an enlarged $\sqrt{3} \times \sqrt{3}$ unit cell. This SDW phase exhibits a 120° AFM

order in the yz plane on each sublattice of the honeycomb. The chiralities of the two 120° AFM orders are opposite. For the tdbWSe₂-realized honeycomb lattice, $t_2/t_1 < 1/3$ for twist angle $\theta < 4^\circ$. Hence, restricted to only on-site interactions, the canted Néel AFM insulator is the most relevant in-plane-field-induced phase for this material at hole filling $\nu = 2$.

In addition to the NNN hopping t_2 , we also study the effect of the NN Hubbard interaction U_1 . We present the phase diagram obtained from the Hartree-Fock calculation as a function of U_0 and U_1 as shown in Fig. 3(c). For this phase diagram, we set $t_2 = 0$ for simplicity. The canted Néel AFM insulator is robust at small U_1 . As U_1 increases, the system is driven to an insulating phase with the charge distribution polarized to one of the sublattices, spontaneously breaking the system's C_{2y} symmetry. In contrast to the canted Néel AFM insulator, the yz -plane $U(1)$ spin rotation symmetry is preserved in this phase. The phase boundary between the AFM insulator and the sublattice-polarized insulator is roughly at $U_1 \sim \frac{1}{3}U_0 + \frac{2}{3}h_x$. This is the exact phase boundary in the strong-interaction limit (where the hopping terms H_h are neglected). In the tdbWSe₂-realized honeycomb lattice, the screening of the Coulomb interaction determines the relative strength between U_0 and U_1 . Stronger screening favors the canted Néel AFM insulator, while weaker screening favors the sublattice-polarized insulator. In Appendix B, we present an analytical mean-field analysis in the weak-coupling limit $U_{0,1} \ll t_1$ and find that the canted $\sqrt{3} \times \sqrt{3}$ SDW insulator can also compete with the canted Néel AFM insulator when U_1/U_0 increases.

IV. SUMMARY AND EXPERIMENTAL IMPLICATIONS

In summary, we show that the ABBA-stacked tdbWSe₂ can serve as a realistic and tunable platform to simulate a Γ -valley honeycomb lattice with both sublattice and $SU(2)$ spin rotation symmetries. We develop a continuum model to

estimate the relevant hopping parameters of this honeycomb lattice model, including the NN and the NNN hoppings t_1 and t_2 . The small bandwidth, found to be at the meV scale, and the ratio t_2/t_1 are both tunable via the twist angle θ . We show that the small bandwidth enables the effective control of the electronic structure via an in-plane magnetic field. At a hole filling $\nu = 2$, an in-plane field of a few tesla can dope this system from a Dirac semimetal to a metal having finite Fermi surfaces with instabilities. To demonstrate this tunability and understand the resulting instabilities, we construct an extended Hubbard model for this honeycomb lattice and perform a numerical Hartree-Fock calculation for the ground-state phase diagram at $\nu = 2$. We find a robust canted Néel AFM insulating phase when the on-site Hubbard interaction U_0 dominates. This phase is conceptually similar to the magnetic-field-induced canted AFM insulator studied in the context of graphene in Ref. [3]. However, our finding resides in a more realistic parameter regime. Moreover, a competing sublattice-polarized insulator is found in our extended Hubbard model when the NN Hubbard interaction U_1 increases beyond a threshold.

The results presented in this paper have direct experimental implications. First, for ABBA-stacked tdbWSe₂ at hole filling $\nu = 2$, an in-plane magnetic field is predicted to induce an insulating ground state. There are two possible insulating ground states: the canted Néel AFM insulator and the sublattice-polarized insulator. The former can be detected through its spin texture perpendicular to the in-plane field direction, potentially using spin-polarized scanning tunneling microscopy [38]. The finite-temperature phase transition into the canted Néel AFM order is a Berezinskii-Kosterlitz-Thouless transition associated with the remaining U(1) spin rotation symmetry under the in-plane field. This metal-insulator transition can be accessed by lowering the temperature at a given in-plane field or by increasing the in-plane field at a low temperature starting from the Dirac semimetal. To be more precise, at zero temperature (and in the absence of disorder), there should be no threshold for the interaction strength or in-plane magnetic field: As long as they are both finite, the insulator phase exists. However, at a finite temperature, one has to turn on an in-plane field and interaction strength beyond certain thresholds to observe the insulating phase with the spin orders. The thresholds can be estimated by comparing the temperature with the gap sizes of the insulating phase at zero temperature. Therefore, at sufficiently low temperature, one can access a metal-insulator transition using an in-plane magnetic field. The sublattice-polarized insulator has no nontrivial spin texture (other than the magnetization along the in-plane field direction). Instead, the spontaneous charge polarization in the two sublattices of the emergent honeycomb lattice leads to a finite electric polarization in the tdbWSe₂ sample along the z direction. Consequently, a signature of this sublattice-polarized insulating phase is the hysteresis of the z -axis electric polarization as a function of the z -direction electric field. The finite-temperature phase transition into the sublattice-polarized phase is in the Ising universality class. Switching between the two insulating phases can be implemented by tuning the ratio between U_0 and U_1 , which is achievable via adjusting the twist angle and/or the sample's distance from the gates.

ACKNOWLEDGMENTS

We thank K. Fai Mak, J. Shan, and L. Ma for stimulating discussions. H.P. acknowledges helpful discussions with Fengcheng Wu, Ming Xie, and Dan Mao. H.P. and E.-A.K. acknowledge funding support from the National Science Foundation [Platform for the Accelerated Realization, Analysis, and Discovery of Interface Materials (PARADIM)] under Cooperative Agreement No. DMR-1539918. C.-M.J. is supported by a faculty startup grant at Cornell University.

APPENDIX A: BAND STRUCTURE CALCULATION AND PARAMETER ESTIMATE

To show that criteria (1) and (3) introduced in the main text can be satisfied by the tdbWSe₂, the first task is to obtain its band structure. However, it is not easy to derive the band structure of tdbWSe₂ directly at the atomic level because the emergent moiré superlattice contains up to 10 000 atoms even within just one moiré unit cell. One way to approximate the band structure of the twisted system is to use a continuum model with parameters fitted according to the untwisted system in the high-symmetry stacking configurations (MM , MX , and XM) that appear in the moiré unit cell of the twisted system [36]. We will provide the details later in this Appendix. Therefore, in this Appendix, we will first discuss the method to obtain the band structure of untwisted systems.

We calculate the band structure of the untwisted system using the *ab initio* tight-binding Hamiltonian [34]. The logic is to first construct a tight-binding model for the monolayer by considering five d orbitals of one tungsten atom and six p orbitals of the two selenium atoms in the monolayer unit cell, and including spin-orbit coupling over the entire monolayer Brillouin zone (BZ) (i.e., not just the small mBZ). It is called *ab initio* because hopping parameters are evaluated from the density functional theory. After constructing the tight-binding model for the monolayer, we can model the interlayer tunneling between the adjacent layers by considering the hopping between the two selenium atoms on the adjacent layers. Combining these considerations, we can construct the Hamiltonian for the (untwisted) double bilayer WSe₂. Finally, we diagonalize the matrix of size 88×88 (11 orbitals \times 2 spins \times 4 layers) at each momentum to obtain the band structure $E_r(k)$, where $r = \{MM, XM, MX\}$ represents the high-symmetry stacking configuration and k is the momentum in the entire monolayer BZ. For the full recipe and the numerical details, we refer the reader to Ref. [34].

Our goal is to show that tdbWSe₂ can satisfy criteria (1) and (3) so that a honeycomb lattice with both sublattice and SU(2) spin rotation symmetries emerges at the moiré scale. That is to say, we require $E_r(\Gamma) > E_r(K)$ for $r = MM, MX$, and XM , and $E_{MX}(\Gamma) = E_{XM}(\Gamma) > E_{MM}(\Gamma)$. Obtaining these energies from the model above requires us to make a choice for the interlayer distances in the tdbWSe₂ structure, which are unknown parameters. Our main goal is to demonstrate the possibility and the tunability of the emergent honeycomb lattice from tdbWSe₂ and estimate the relevant energy scale. We will not attempt to calculate the relaxed interlayer distances. Instead, we will make assumptions on them based on the following reasoning. In light of the C_{2y} symmetry which flips

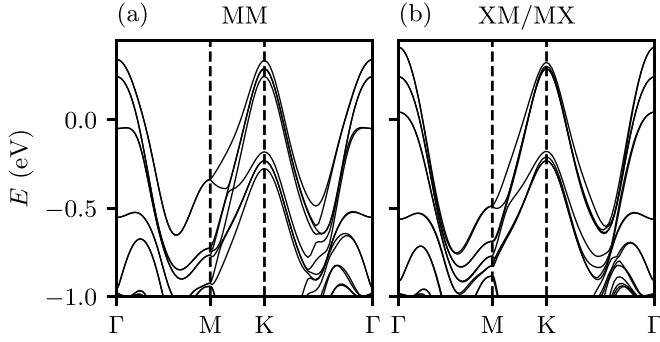


FIG. 4. The valence band of tdbWSe₂ in the monolayer Brillouin zone for (a) the *MM* stacking configuration and (b) the *MX* and *XM* stacking configurations.

the layers, the distance d_{12} between the first and second layers should be the same as the distance d_{34} between the third and fourth layers. For the distance between the central two layers d_{23} , because the *MM* stacking corresponds to the case where all tungsten atoms (also for selenium atoms) on both layers are stacked with perfect alignment, respectively, the repulsion from the interlayer interaction should be the strongest. Therefore the value of d_{23} in the *MM* stacking configuration should be larger than d_{12} and d_{23} in the *MX* and *XM* stacking configurations. With these considerations, we perturb the interlayer distances d_{12} and d_{23} for the *MM* stacking and the interlayer distance d_{23} for the *MX* and *XM* stacking, around the interlayer distance from the bulk WSe₂ data, ~ 6.5 Å [35], and find that the system can satisfy the energetics hierarchy in criteria (1) and (3) in a large parameter space around $d_{12} = 6$ Å. As an example that passes criteria (1) and (3), we choose the following interlayer distances: $(d_{12}, d_{23}, d_{34}) = (6, 6.25, 6)$ Å for *MM* stacking and $(d_{12}, d_{23}, d_{34}) = (6, 5.8, 6)$ Å for *MX* and *XM* stacking for the estimation of the parameters in the continuum model. Note that this choice has smaller layer distances than the bulk data. In principle, one can consider adding pressure to reduce the interlayer distance if needed. For example, a range of d_{23} from 6 to 6.5 Å (from 5.7 to 6.3 Å) for *MM* (*MX* and *XM*) stacking with $d_{23} = 5.8$ Å ($d_{23} = 6.25$ Å) for *MX* and *XM* (*MM*) stacking fixed can also satisfy both criteria.

Now, we present the valence band structure for the untwisted *MM* stacking in Fig. 4(a) and for untwisted *MX* and *XM* stacking in Fig. 4(b). The corresponding valence band edge energies at the Γ and K valleys for these two stackings, listed in Table I, validate the two criteria.

TABLE I. First four valence band (from the top to bottom) energies (eV) at the Γ and K valleys for *MM* stackings and for *MX* and *XM* stackings.

Band	$E_{MM}(\Gamma)$	$E_{MX-XM}(\Gamma)$	$E_{MM}(K)$	$E_{MX-XM}(K)$
0	0.341112	0.410080	0.334569	0.323034
1	0.244373	0.242830	0.286263	0.289225
2	-0.050321	0.042969	-0.182268	-0.179475
3	-0.553378	-0.564056	-0.232956	-0.232795

To model the twisted moiré system from the untwisted system, we can represent the energy at the high-symmetry-stacking sites in one moiré unit cell using the energies in an untwisted system with the same type of stacking configuration. Then we interpolate them using up to the first harmonics of the moiré periodicity [36]. Therefore, by extracting the four topmost valence bands at the Γ valley for the untwisted systems in the *MM*, *MX*, and *XM* stacking configurations, we can estimate the unknown parameters in the moiré continuum Hamiltonian equation (1) in the twisted system. To do that, we first will drop the kinetic term in Eq. (1), as it is near the Γ valley, and then diagonalize the potential term with $r = MM$ and $r = MX$ or *XM*, respectively, which gives four discrete energies for each site. The fitting procedure is to adjust these four energies at $r = MM$ or $r = MX$ or *XM* to match the energies obtained from the four valence bands in the *ab initio* tight-binding Hamiltonian at the Γ valley, i.e., the first two columns in Table I.

APPENDIX B: PHASE COMPETITION IN THE WEAK-INTERACTION LIMIT

In this Appendix, we present the analytical mean-field study of the Fermi surface instabilities in our extended Hubbard model (with the in-plane magnetic field) in the weak-coupling limit $U_{0,1} \ll t_1$ at hole filling $\nu = 2$. We find that, at zero temperature, dominant instabilities include both the canted Néel AFM order and the canted $\sqrt{3} \times \sqrt{3}$ SDW order. Their competition is controlled by the ratio U_1/U_0 . We also discuss the relationship between our weak-coupling analysis and the Hartree-Fock phase diagrams in Fig. 3 obtained in the stronger coupling regime $U_0 \gtrsim t_1$.

We start with the noninteracting part of the Hamiltonian $H^0 = H_h + H_Z$ containing the hopping term and the Zeeman energy. At hole filling $\nu = 2$, for small t_2 and h_x compared with t_1 , the Fermi surfaces are centered at the κ and κ' points of the mBZ. We expand the dispersion around the κ or κ' point:

$$H_{\kappa,\sigma}^0 = \sum_{\mathbf{k}} \tilde{c}_{\kappa,\sigma}^\dagger(\mathbf{k})(h_x\sigma\Lambda^0 + v_F\vec{\Lambda} \cdot \mathbf{k})\tilde{c}_{\kappa,\sigma}(\mathbf{k}),$$

$$H_{\kappa',\sigma}^0 = \sum_{\mathbf{k}} \tilde{c}_{\kappa',\sigma}^\dagger(\mathbf{k})(h_x\sigma\Lambda^0 - v_F\vec{\Lambda}^* \cdot \mathbf{k})\tilde{c}_{\kappa',\sigma}(\mathbf{k}). \quad (\text{B1})$$

Here, \mathbf{k} is the momentum measured from the κ or κ' point. The dispersion is expanded to the linear order of \mathbf{k} , which suffices to study the Fermi surface instabilities. The Fermi velocity $v_F = \sqrt{3}/2|t_1|a_M$, which is $\sim 2.2 \times 10^4$ m/s at a twist angle of $\theta = 2^\circ$. $\tilde{c}_{\tau,\sigma} = [c_{\tau,A,\sigma}, c_{\tau,B,\sigma}]^T$ is the fermionic spinor in the sublattice space at valley $\tau = \kappa$ or κ' with spin $\sigma = \uparrow, \downarrow$ along the in-plane field direction \hat{x} . $\vec{\Lambda}$ comprises the Pauli-X and Y matrices acting on the sublattice space. Note that t_2 's contribution only starts to appear in the order- \mathbf{k}^2 terms of the dispersion. This contribution is independent of valley, spin, and sublattice. Hence a small t_2 is unimportant for the Fermi surface instability in the weak-coupling limit.

At nonzero h_x , the Fermi surfaces of the spin-up fermions are perfectly nested with those of the spin-down fermions. Consequently, particle-hole instabilities towards magnetic ground states with spontaneous hybridization between the

two spin species are expected. The magnetic orders in these ground states spontaneously break the U(1) spin rotation symmetry in the yz plane (perpendicular to the in-plane field direction). In the limit $h_x \rightarrow 0$, the instabilities towards such magnetically ordered ground states vanish along with the Fermi surfaces in the noninteracting band structure. Hence these magnetic orders, to be discussed in detail below, are dubbed *in-plane-field-induced* magnetic orders.

At hole filling $\nu = 2$ (and with finite $h_x > 0$), we begin our analysis of possible instabilities by writing down the noninteracting bands crossing the Fermi level:

$$H_\tau = \sum_{\mathbf{k}} E_{+, \downarrow}(\mathbf{k}) c_{\tau, +, \downarrow}^\dagger(\mathbf{k}) c_{\tau, +, \downarrow}(\mathbf{k}) + E_{-, \uparrow}(\mathbf{k}) c_{\tau, -, \uparrow}^\dagger(\mathbf{k}) c_{\tau, -, \uparrow}(\mathbf{k}), \quad (\text{B2})$$

for the two valleys $\tau = \kappa, \kappa'$ and the two spin species $\sigma = \uparrow, \downarrow$. The energies $E_{\pm, \sigma}(\mathbf{k})$ are given by $E_{\pm, \sigma}(\mathbf{k}) = h_x \sigma \pm v_F |\mathbf{k}|$ with \pm playing the role of a band index. This band index \pm is locked with the spin index σ for the bands that cross the

Fermi level. The fermion operators $c_{\tau, \pm, \sigma}$ are defined as

$$\begin{pmatrix} c_{\kappa, +, \sigma}^\dagger(\mathbf{k}) \\ c_{\kappa, -, \sigma}^\dagger(\mathbf{k}) \end{pmatrix} = \frac{1}{\sqrt{2}} \begin{pmatrix} 1 & e^{i\theta(\mathbf{k})} \\ 1 & -e^{i\theta(\mathbf{k})} \end{pmatrix} \begin{pmatrix} c_{\kappa, A, \sigma}^\dagger(\mathbf{k}) \\ c_{\kappa, B, \sigma}^\dagger(\mathbf{k}) \end{pmatrix} \quad (\text{B3})$$

and

$$\begin{pmatrix} c_{\kappa', +, \sigma}^\dagger(\mathbf{k}) \\ c_{\kappa', -, \sigma}^\dagger(\mathbf{k}) \end{pmatrix} = \frac{1}{\sqrt{2}} \begin{pmatrix} -e^{i\theta(\mathbf{k})} & 1 \\ e^{i\theta(\mathbf{k})} & 1 \end{pmatrix} \begin{pmatrix} c_{\kappa', A, \sigma}^\dagger(\mathbf{k}) \\ c_{\kappa', B, \sigma}^\dagger(\mathbf{k}) \end{pmatrix}, \quad (\text{B4})$$

where $\theta(\mathbf{k})$ is the azimuth angle of \mathbf{k} . The spin-up (spin-down) fermions have two particlelike (holelike) Fermi surface pockets, one around the κ point and the other around the κ' point. Hence possible particle-hole instabilities (at weak couplings) can occur through either intervalley or intravalley hybridizations of the two spin species.

First, we consider the intervalley hybridization associated with the mean-field order parameter $\langle c_{\tau, -, \uparrow}^\dagger(\mathbf{k}) c_{\bar{\tau}, +, \downarrow}(\mathbf{k}) \rangle$. Here, $\bar{\tau}$ represents the opposite valley of τ . The mean-field decomposition of the extended Hubbard interaction corresponding to the intervalley hybridization reads

$$H_{\text{int}}^{\text{inter}} = - \sum_{\mathbf{k}, \mathbf{k}', \tau, \sigma} \left(\frac{U_0}{2N} \cos(\theta(\mathbf{k}) - \theta(\mathbf{k}')) + \frac{3U_1}{2N} \right) \langle c_{\bar{\tau}, \bar{\sigma}}^\dagger(\mathbf{k}') c_{\tau, \sigma}(\mathbf{k}') \rangle c_{\tau, \sigma}^\dagger(\mathbf{k}) c_{\bar{\tau}, \bar{\sigma}}(\mathbf{k}) + \sum_{\mathbf{k}, \mathbf{k}', \tau} \left(\frac{U_0}{2N} \cos(\theta(\mathbf{k}) - \theta(\mathbf{k}')) + \frac{3U_1}{2N} \right) \langle c_{\tau, \uparrow}^\dagger(\mathbf{k}') c_{\bar{\tau}, \downarrow}(\mathbf{k}') \rangle \langle c_{\bar{\tau}, \downarrow}^\dagger(\mathbf{k}) c_{\tau, \uparrow}(\mathbf{k}) \rangle. \quad (\text{B5})$$

Here, $\bar{\sigma}$ represents the opposite spin of σ . N is the system size. The band index is suppressed in the shorthand $c_{\tau, \uparrow}(\mathbf{k}) = c_{\tau, -, \uparrow}(\mathbf{k})$ and $c_{\tau, \downarrow}(\mathbf{k}) = c_{\tau, +, \downarrow}(\mathbf{k})$ due to the locking of the spin and the band indices for the bands that cross the Fermi level. In the derivation of $H_{\text{int}}^{\text{inter}}$, the terms irrelevant to the intervalley hybridization of opposite spin species and the terms of linear or higher order in k are dropped. Note that the first (second) term in the quadratic terms in the first line of Eq. (B5) only couples to the p -wave (s -wave) channel of

the order parameter $\langle c_{\tau, -, \uparrow}^\dagger(\mathbf{k}) c_{\bar{\tau}, +, \downarrow}(\mathbf{k}) \rangle$. We can consider the s -wave channel (with orbital angular momentum $|l| = 0$) and the p -wave channel (with orbital angular momentum $|l| = 1$) separately. At the mean-field level, the saddle point equations in the s -wave channel only depend on U_1 , while those in the p -wave channel only depend on U_0 .

For the intravalley hybridization associated with the mean-field order parameter $\langle c_{\tau, -, \uparrow}^\dagger(\mathbf{k}) c_{\tau, +, \downarrow}(\mathbf{k}) \rangle$, the mean-field decomposition of interaction terms reads

$$H_{\text{int}}^{\text{intra}} = - \frac{U_0}{2N} \sum_{\mathbf{k}, \mathbf{k}', \tau, \sigma} (\langle c_{\bar{\tau}, \bar{\sigma}}^\dagger(\mathbf{k}') c_{\tau, \sigma}(\mathbf{k}') \rangle - \langle c_{\bar{\tau}, \bar{\sigma}}^\dagger(\mathbf{k}') c_{\bar{\tau}, \sigma}(\mathbf{k}') \rangle) c_{\tau, \sigma}^\dagger(\mathbf{k}) c_{\bar{\tau}, \bar{\sigma}}(\mathbf{k}) - \frac{3U_1}{2N} \sum_{\mathbf{k}, \mathbf{k}', \tau, \sigma} \cos(\theta(\mathbf{k}) - \theta(\mathbf{k}')) \langle c_{\bar{\tau}, \bar{\sigma}}^\dagger(\mathbf{k}') c_{\tau, \sigma}(\mathbf{k}') \rangle c_{\tau, \sigma}^\dagger(\mathbf{k}) c_{\bar{\tau}, \bar{\sigma}}(\mathbf{k}) + \frac{U_0}{2N} \sum_{\mathbf{k}, \mathbf{k}'} (\langle c_{\kappa, \uparrow}^\dagger(\mathbf{k}') c_{\kappa, \downarrow}(\mathbf{k}') \rangle - \langle c_{\kappa', \uparrow}^\dagger(\mathbf{k}') c_{\kappa', \downarrow}(\mathbf{k}') \rangle) (\langle c_{\kappa, \downarrow}^\dagger(\mathbf{k}) c_{\kappa, \uparrow}(\mathbf{k}) \rangle - \langle c_{\kappa', \downarrow}^\dagger(\mathbf{k}) c_{\kappa', \uparrow}(\mathbf{k}) \rangle) + \frac{3U_1}{2N} \sum_{\mathbf{k}, \mathbf{k}', \tau} \cos(\theta(\mathbf{k}) - \theta(\mathbf{k}')) \langle c_{\tau, \uparrow}^\dagger(\mathbf{k}') c_{\tau, \downarrow}(\mathbf{k}') \rangle \langle c_{\tau, \downarrow}^\dagger(\mathbf{k}) c_{\tau, \uparrow}(\mathbf{k}) \rangle. \quad (\text{B6})$$

Similar to the intervalley case, based on the form of $H_{\text{int}}^{\text{intra}}$, we only need to consider the s -wave and the p -wave channels of the order parameter $\langle c_{\tau, -, \uparrow}^\dagger(\mathbf{k}) c_{\tau, +, \downarrow}(\mathbf{k}) \rangle$. Also, it is natural to expect that the order parameters in the two valleys $\tau = \kappa, \kappa'$ share the same orbital angular momentum. With this

expectation, we find that the saddle point equations in the s -wave channel only depend on U_0 while those in the p -wave channel only depend on U_1 .

At zero temperature, we find the two most dominant mean-field solutions with the largest gaps opened around the Fermi

surface. The corresponding orders are then expected to have the highest mean-field transition temperatures. One of these mean-field solutions is given by the intervalley hybridization in the s -wave channel with $\langle c_{\kappa,-,\uparrow}^\dagger c_{\kappa',+,\downarrow} \rangle = \langle c_{\kappa',-,\uparrow}^\dagger c_{\kappa,+,\downarrow} \rangle$, which gives rise to the canted $\sqrt{3} \times \sqrt{3}$ SDW order, as illustrated in Fig. 3(b). In this phase, the gap opened at the Fermi surface is given by $2h_x \exp(-\frac{2}{3U_1\rho})$, where the density of states ρ can be approximated to a constant $\frac{4h_x}{3\pi t_1^2}$ within the energy interval between two Dirac points (at energies $-h_x$ and h_x relative to the Fermi level). The other dominant mean-field solution is given by the intravalley hybridization in the s -wave channel with $\langle c_{\kappa,-,\uparrow}^\dagger c_{\kappa,+,\downarrow} \rangle = -\langle c_{\kappa',-,\uparrow}^\dagger c_{\kappa',+,\downarrow} \rangle$, which gives rise to the canted Néel AFM order, as shown in Figs. 3(b) and 3(c). In this canted Néel AFM phase, the gap size is given by $2h_x \exp(-\frac{1}{U_0\rho})$.

By comparing the gaps, we expect the canted Néel AFM phase to be the energetically favorable ground state for

$U_1 < \frac{2}{3}U_0$ in the weak-coupling limit. When U_1 increases beyond $\frac{2}{3}U_0$, the ground state goes through a first-order phase transition into the canted $\sqrt{3} \times \sqrt{3}$ SDW phase. We comment that it is challenging to extend our numerical Hartree-Fock calculation, which includes all the interaction terms, to the weak-coupling limit because of the exponentially small gap sizes. From the Hartree-Fock phase diagram with $U_0 > t_1$ as shown in Fig. 3(c), the sublattice-polarized phase is more energetically favorable than both the canted $\sqrt{3} \times \sqrt{3}$ SDW insulator and the canted Néel AFM insulator when $U_1 \gtrsim \frac{1}{3}U_0 + \frac{2}{3}h_x$. However, there is no Fermi surface instability towards the sublattice-polarized insulator in the weak-coupling limit. It would be interesting to investigate the competition between the canted Néel AFM insulator, the $\sqrt{3} \times \sqrt{3}$ SDW insulator, and the sublattice-polarized insulator in the regime with $U_0 < t_1$, which we will leave for future study.

-
- [1] C. Honerkamp, Density waves and Cooper pairing on the honeycomb lattice, *Phys. Rev. Lett.* **100**, 146404 (2008).
- [2] I. L. Aleiner, D. E. Kharzeev, and A. M. Tsvelik, Spontaneous symmetry breaking in graphene subjected to an in-plane magnetic field, *Phys. Rev. B* **76**, 195415 (2007).
- [3] M. Bercx, T. C. Lang, and F. F. Assaad, Magnetic field induced semimetal-to-canted-antiferromagnet transition on the honeycomb lattice, *Phys. Rev. B* **80**, 045412 (2009).
- [4] R. Nandkishore, L. S. Levitov, and A. V. Chubukov, Chiral superconductivity from repulsive interactions in doped graphene, *Nat. Phys.* **8**, 158 (2012).
- [5] R. Nandkishore, R. Thomale, and A. V. Chubukov, Superconductivity from weak repulsion in hexagonal lattice systems, *Phys. Rev. B* **89**, 144501 (2014).
- [6] S. Raghu, X.-L. Qi, C. Honerkamp, and S.-C. Zhang, Topological Mott insulators, *Phys. Rev. Lett.* **100**, 156401 (2008).
- [7] E. C. Regan, D. Wang, C. Jin, M. I. Bakti Utama, B. Gao, X. Wei, S. Zhao, W. Zhao, Z. Zhang, K. Yumigeta, M. Blei, J. D. Carlström, K. Watanabe, T. Taniguchi, S. Tongay, M. Crommie, A. Zettl, and F. Wang, Mott and generalized Wigner crystal states in WSe₂/WS₂ moiré superlattices, *Nature (London)* **579**, 359 (2020).
- [8] Y. Tang, L. Li, T. Li, Y. Xu, S. Liu, K. Barmak, K. Watanabe, T. Taniguchi, A. H. MacDonald, J. Shan, and K. F. Mak, Simulation of Hubbard model physics in WSe₂/WS₂ moiré superlattices, *Nature (London)* **579**, 353 (2020).
- [9] Y. Xu, S. Liu, D. A. Rhodes, K. Watanabe, T. Taniguchi, J. Hone, V. Elser, K. F. Mak, and J. Shan, Correlated insulating states at fractional fillings of moiré superlattices, *Nature (London)* **587**, 214 (2020).
- [10] L. Wang, E.-M. Shih, A. Ghiotto, L. Xian, D. A. Rhodes, C. Tan, M. Claassen, D. M. Kennes, Y. Bai, B. Kim, K. Watanabe, T. Taniguchi, X. Zhu, J. Hone, A. Rubio, A. N. Pasupathy, and C. R. Dean, Correlated electronic phases in twisted bilayer transition metal dichalcogenides, *Nat. Mater.* **19**, 861 (2020).
- [11] A. Ghiotto, E.-M. Shih, G. S. S. G. Pereira, D. A. Rhodes, B. Kim, J. Zang, A. J. Millis, K. Watanabe, T. Taniguchi, J. C. Hone, L. Wang, C. R. Dean, and A. N. Pasupathy, Quantum criticality in twisted transition metal dichalcogenides, *Nature (London)* **597**, 345 (2021).
- [12] Y. Zhou, J. Sung, E. Brutschea, I. Esterlis, Y. Wang, G. Scuri, R. J. Gelly, H. Heo, T. Taniguchi, K. Watanabe, G. Zaránd, M. D. Lukin, P. Kim, E. Demler, and H. Park, Bilayer Wigner crystals in a transition metal dichalcogenide heterostructure, *Nature (London)* **595**, 48 (2021).
- [13] H. Li, S. Li, E. C. Regan, D. Wang, W. Zhao, S. Kahn, K. Yumigeta, M. Blei, T. Taniguchi, K. Watanabe, S. Tongay, A. Zettl, M. F. Crommie, and F. Wang, Imaging two-dimensional generalized Wigner crystals, *Nature (London)* **597**, 650 (2021).
- [14] T. Li, S. Jiang, B. Shen, Y. Zhang, L. Li, Z. Tao, T. Devakul, K. Watanabe, T. Taniguchi, L. Fu, J. Shan, and K. F. Mak, Quantum anomalous Hall effect from intertwined moiré bands, *Nature (London)* **600**, 641 (2021).
- [15] J. Gu, L. Ma, S. Liu, K. Watanabe, T. Taniguchi, J. C. Hone, J. Shan, and K. F. Mak, Dipolar excitonic insulator in a moiré lattice, *Nat. Phys.* **18**, 395 (2022).
- [16] W. Zhao, K. Kang, L. Li, C. Tschirhart, E. Redekop, K. Watanabe, T. Taniguchi, A. Young, J. Shan, and K. F. Mak, Realization of the Haldane Chern insulator in a moiré lattice, *arXiv:2207.02312*.
- [17] Y.-M. Xie, C.-P. Zhang, J.-X. Hu, K. F. Mak, and K. T. Law, Valley-polarized quantum anomalous Hall state in moiré MoTe₂/WSe₂ heterobilayers, *Phys. Rev. Lett.* **128**, 026402 (2022).
- [18] Y.-M. Xie, C.-P. Zhang, and K. T. Law, Topological $p_x + ip_y$ inter-valley coherent state in moiré MoTe₂/WSe₂ heterobilayers, *arXiv:2206.11666*.
- [19] Z. Tao, B. Shen, S. Jiang, T. Li, L. Li, L. Ma, W. Zhao, J. Hu, K. Pistunova, K. Watanabe, T. Taniguchi, T. F. Heinz, K. F. Mak, and J. Shan, Valley-coherent quantum anomalous Hall state in AB-stacked MoTe₂/WSe₂ bilayers, *arXiv:2208.07452*.
- [20] E. Liu, T. Taniguchi, K. Watanabe, N. M. Gabor, Y.-T. Cui, and C. H. Lui, Excitonic and valley-polarization signatures of fractional correlated electronic phases in a WSe₂/WS₂ moiré superlattice, *Phys. Rev. Lett.* **127**, 037402 (2021).

- [21] B. A. Foutty, C. R. Kometter, T. Devakul, A. P. Reddy, K. Watanabe, T. Taniguchi, L. Fu, and B. E. Feldman, Mapping twist-tuned multi-band topology in bilayer WSe₂, [arXiv:2304.09808](#).
- [22] Y. Zhang, T. Devakul, and L. Fu, Spin-textured Chern bands in AB-stacked transition metal dichalcogenide bilayers, *Proc. Natl. Acad. Sci. USA* **118**, e2112673118 (2021).
- [23] F. Wu, T. Lovorn, E. Tutuc, I. Martin, and A. H. MacDonald, Topological insulators in twisted transition metal dichalcogenide homobilayers, *Phys. Rev. Lett.* **122**, 086402 (2019).
- [24] M. Angeli and A. H. MacDonald, Γ valley transition metal dichalcogenide moiré bands, *Proc. Natl. Acad. Sci. USA* **118**, e2021826118 (2021).
- [25] Y. Zhang, T. Liu, and L. Fu, Electronic structures, charge transfer, and charge order in twisted transition metal dichalcogenide bilayers, *Phys. Rev. B* **103**, 155142 (2021).
- [26] L. Xian, M. Claassen, D. Kiese, M. M. Scherer, S. Trebst, D. M. Kennes, and A. Rubio, Realization of nearly dispersionless bands with strong orbital anisotropy from destructive interference in twisted bilayer MoS₂, *Nat. Commun.* **12**, 5644 (2021).
- [27] H. C. P. Movva, T. Lovorn, B. Fallahzad, S. Larentis, K. Kim, T. Taniguchi, K. Watanabe, S. K. Banerjee, A. H. MacDonald, and E. Tutuc, Tunable $\Gamma - K$ valley populations in hole-doped trilayer WSe₂, *Phys. Rev. Lett.* **120**, 107703 (2018).
- [28] H. Pan, F. Wu, and S. Das Sarma, Band topology, Hubbard model, Heisenberg model, and Dzyaloshinskii-Moriya interaction in twisted bilayer WSe₂, *Phys. Rev. Res.* **2**, 033087 (2020).
- [29] G. Gatti, J. Issing, L. Rademaker, F. Margot, T. A. de Jong, S. J. van der Molen, J. Teyssier, T. K. Kim, M. D. Watson, C. Cacho, P. Dudin, J. Avila, K. C. Edwards, P. Paruch, N. Ubrig, I. Gutiérrez-Lezama, A. Morpurgo, A. Tamai, and F. Baumberger, Flat Γ moiré bands in twisted bilayer WSe₂, *Phys. Rev. Lett.* **131**, 046401 (2023).
- [30] D. Pei, B. Wang, Z. Zhou, Z. He, L. An, S. He, C. Chen, Y. Li, L. Wei, A. Liang, J. Avila, P. Dudin, V. Kandyba, A. Giampietri, M. Cattelan, A. Barinov, Z. Liu, J. Liu, H. Weng, N. Wang *et al.*, Observation of Γ -valley moiré bands and emergent hexagonal lattice in twisted transition metal dichalcogenides, *Phys. Rev. X* **12**, 021065 (2022).
- [31] B. A. Foutty, J. Yu, T. Devakul, C. R. Kometter, Y. Zhang, K. Watanabe, T. Taniguchi, L. Fu, and B. E. Feldman, Tunable spin and valley excitations of correlated insulators in Γ -valley moiré bands, *Nat. Mater.* **22**, 731 (2023).
- [32] K. F. Mak, C. Lee, J. Hone, J. Shan, and T. F. Heinz, Atomically thin MoS₂: A new direct-gap semiconductor, *Phys. Rev. Lett.* **105**, 136805 (2010).
- [33] X. Xu, W. Yao, D. Xiao, and T. F. Heinz, Spin and pseudospins in layered transition metal dichalcogenides, *Nat. Phys.* **10**, 343 (2014).
- [34] S. Fang, R. Kuate Defo, S. N. Shirodkar, S. Lieu, G. A. Tritsarlis, and E. Kaxiras, *Ab initio* tight-binding Hamiltonian for transition metal dichalcogenides, *Phys. Rev. B* **92**, 205108 (2015).
- [35] J. He, K. Hummer, and C. Franchini, Stacking effects on the electronic and optical properties of bilayer transition metal dichalcogenides MoS₂, MoSe₂, WS₂, and WSe₂, *Phys. Rev. B* **89**, 075409 (2014).
- [36] J. Jung, A. Raoux, Z. Qiao, and A. H. MacDonald, *Ab initio* theory of moiré superlattice bands in layered two-dimensional materials, *Phys. Rev. B* **89**, 205414 (2014).
- [37] J. Jung and A. H. MacDonald, Tight-binding model for graphene π -bands from maximally localized Wannier functions, *Phys. Rev. B* **87**, 195450 (2013).
- [38] O. Pietzsch, A. Kubetzka, M. Bode, and R. Wiesendanger, Observation of magnetic hysteresis at the nanometer scale by spin-polarized scanning tunneling spectroscopy, *Science* **292**, 2053 (2001).